



HAL
open science

Effect of surface nano/micro-structuring on the early formation of microbial anodes with *Geobacter sulfurreducens*: Experimental and theoretical approaches

Pierre Champigneux, Cyril Renault-Sentenac, David Bourrier, Carole Rossi, Marie-Line Délia-Dupuy, Alain Bergel

► To cite this version:

Pierre Champigneux, Cyril Renault-Sentenac, David Bourrier, Carole Rossi, Marie-Line Délia-Dupuy, et al.. Effect of surface nano/micro-structuring on the early formation of microbial anodes with *Geobacter sulfurreducens*: Experimental and theoretical approaches. *Bioelectrochemistry*, 2018, 121 (121), pp.191-200. 10.1016/j.bioelechem.2018.02.005 . hal-01713422

HAL Id: hal-01713422

<https://laas.hal.science/hal-01713422v1>

Submitted on 21 Jan 2019

HAL is a multi-disciplinary open access archive for the deposit and dissemination of scientific research documents, whether they are published or not. The documents may come from teaching and research institutions in France or abroad, or from public or private research centers.

L'archive ouverte pluridisciplinaire **HAL**, est destinée au dépôt et à la diffusion de documents scientifiques de niveau recherche, publiés ou non, émanant des établissements d'enseignement et de recherche français ou étrangers, des laboratoires publics ou privés.






Open Archive Toulouse Archive Ouverte

OATAO is an open access repository that collects the work of Toulouse researchers and makes it freely available over the web where possible

This is an author's version published in: <http://oatao.univ-toulouse.fr/21108>

Official URL: <https://doi.org/10.1016/j.bioelechem.2018.02.005>

To cite this version:

Champigneux, Pierre  and Renault-Sentenac, Cyril and Bourrier, David and Rossi, Carole and Délia, Marie-Line  and Bergel, Alain  *Effect of surface nano/micro-structuring on the early formation of microbial anodes with Geobacter sulfurreducens : Experimental and theoretical approaches.* (2018) Bioelectrochemistry, 121. 191-200. ISSN 1567-5394

Any correspondence concerning this service should be sent to the repository administrator: tech-oatao@listes-diff.inp-toulouse.fr

Effect of surface nano/micro-structuring on the early formation of microbial anodes with *Geobacter sulfurreducens*: Experimental and theoretical approaches

Pierre Champigneux^{a,*}, Cyril Renault-Sentenac^b, David Bourrier^b, Carole Rossi^b, Marie-Line Delia^a, Alain Bergel^a

^a Laboratoire de Génie Chimique CNRS - Université de Toulouse (INPT), 4 allée Emile Monso, 31432 Toulouse, France

^b Laboratoire d'Analyse et d'Architecture des Systèmes CNRS - Université de Toulouse, 7 avenue du colonel Roche, 31031 Toulouse, France

A B S T R A C T

Smooth and nano rough flat gold electrodes were manufactured with controlled Ra of 0.8 and 4.5 nm, respectively. Further nano rough surfaces (Ra 4.5 nm) were patterned with arrays of micro pillars 500 μm high. All these electrodes were implemented in pure cultures of *Geobacter sulfurreducens*, under a constant potential of 0.1 V/SCE and with a single addition of acetate 10 mM to check the early formation of microbial anodes. The flat smooth electrodes produced an average current density of $0.9 \text{ A}\cdot\text{m}^{-2}$. The flat nano rough electrodes reached $2.5 \text{ A}\cdot\text{m}^{-2}$ on average, but with a large experimental deviation of $\pm 2.0 \text{ A}\cdot\text{m}^{-2}$. This large deviation was due to the erratic colonization of the surface but, when settled on the surface, the cells displayed current density that was directly correlated to the biofilm coverage ratio.

The micro pillars considerably improved the experimental reproducibility by offering the cells a quieter environment, facilitating biofilm development. Current densities of up to $8.5 \text{ A}\cdot\text{m}^{-2}$ (per projected surface area) were thus reached, in spite of rate limitation due to the mass transport of the buffering species, as demonstrated by numerical modelling. Nano roughness combined with micro structuring increased current density by a factor close to 10 with respect to the smooth flat surface.

Keywords:

Bioanode
Surface roughness
Microbial adhesion
Microbial fuel cell
Modelling

1. Introduction

For around two decades, microbial anodes have been opening up fascinating avenues for a huge number of electrochemical processes [1–3]. Microbial fuel cells (MFCs) were the pioneering systems in which microbial anodes were implemented [4,5] and they have since been the source of numerous innovative technological concepts, such as microbial electrolysis cells for hydrogen production [6,7] metal recovery [8,9], microbial autonomous biosensors [10,11] and a microbial snorkel for environmental bioremediation [12,13].

Biofilm development on an electrode surface can be described in three steps: initial reversible contact between cells and the surface, followed by irreversible cell attachment and, finally, biofilm growth due to bacterial division and extracellular matrix production [14,15]. In each of these phases, biofilm formation is strongly dependent on the surface/bacteria interaction.

Many studies have pointed out the electrode surface topography as a key parameter of the efficiency of microbial electrodes [16–20]. Roughness has often been used to investigate the effects of surface topography but it remains difficult to extract clear trends, most likely because of the different techniques that have been used to roughen the electrode surfaces, which did not allow direct comparison among the studies [21–23].

Some research teams have structured surfaces by using the accurate tools provided by nano and micro technologies in order to control the surface topography perfectly. Amazing advances have been made in this way. Titanium nanowires and nanotubes have been shown to improve the performance of electroactive biofilms by acting as substitutes for bacterial pili [24–26]. Recessed micro structures, such as holes, revealed a positive effect due to the increased contact area between the cell and the electrode surface, when they were the same size as the cell. Nevertheless, as a side effect, holes that are too deep can induce detrimental segmentation of the biofilm [27–29]. Protuberant micro structures, such as pillars, do not present this drawback. Gold cross shaped micro pillars 40 μm wide and 8 μm high inoculated with *S. cerevisiae* have shown a 4.9 fold increase in current density, mainly explained by an increase of the electrode surface area to volume ratio by a factor of

* Corresponding author.

E-mail addresses: pierre.champigneux@ensiacet.fr (P. Champigneux), alain.bergel@ensiacet.fr (A. Bergel).

4.5 [30]. Microbial anodes manufactured with 20 μm high and 20 μm diameter cylindrical micro pillars and inoculated with *S. marcescens* have displayed a 1.5 fold increase of the current density [31].

Most of these studies have delivered worthwhile conclusions on mature biofilms. In contrast, almost nothing is known about the mechanism of the early phases of the formation of electroactive biofilms, in which the surface topography should have a crucial impact on the initial steps of biofilm formation. Moreover, it can also be presumed that the final electrocatalytic properties of a biofilm depend strongly on its early formation phases, which establish the interfacial layer between the electrode surface and the biofilm [32].

The purpose of the present study was to gain insight into the impact of surface topography on the early phases of electroactive biofilm formation. Micro technology techniques were implemented to control the surface roughness of gold electrodes perfectly at the nanometre level and then to pattern the surface with arrays of micro pillars. Gold was chosen as the electrode material because of its suitability for implementing micro technology techniques and because it has been demonstrated to be fully able to support the formation of efficient microbial anodes [16,30,33–36]. Micro structuring of the surfaces was performed with micro pillars having a square cross section. Their height of 500 μm was significantly greater than those generally reported in the literature so far, in order to maximize the chances of detecting their impact.

Many bacteria have been found to possess electrocatalytic properties [37]. Among the models of electroactive bacteria, *Geobacter sulfurreducens* [38] has been widely used and has shown one of the highest levels of performance in terms of current production in pure culture [39,40]. For this reason, this species was chosen for the present study.

2. Materials and methods

2.1. Electrode manufacturing

Smooth gold (SG) and Nano rough gold (NG) electrodes were formed on Si (100), P type silica wafers. The SG surfaces were deposited by evaporation of a 250 nm thick gold layer. The NG electrodes were produced by roughening the surface of SG electrodes by electrolytic deposition of gold to achieve a gold layer 1.75 μm thick. The average roughness, measured by AFM was 0.8 nm for the SG surfaces and 4.5 nm for the NG.

Surface micro structuring consisted of arrays of square micro pillars 100 μm wide and 500 μm high. They were created on the same Si (100), P type silica wafers with an epoxy resin (SU 8 3050, MicroChem Corp) patterned by photolithography to form the pillar array. Electrode metalization was performed by electrolytic deposition of gold as for the NG electrodes. A 1 μm thick gold layer was thus created, with a roughness of 4.5 nm identical to that of the NG electrodes. The different pillar arrays were obtained with spacings of 100 μm ($\mu\text{P}100\text{NG}$), 125 μm ($\mu\text{P}125\text{NG}$) and 200 μm ($\mu\text{P}200\text{NG}$). The three micro structured electrodes had 2500, 2025 and 1156 pillars and an overall geometric surface area of 5.73, 5.03 and 3.26 cm^2 , respectively. Each pillar array was tested in duplicate.

2.2. Inocula and media

Geobacter sulfurreducens (ATCC 51573) was purchased from DSMZ. The specific growth medium contained, per litre: 0.1 g KCl, 1.5 g NH_4Cl , 2.5 g NaHCO_3 , 0.6 g NaH_2PO_4 , and 0.82 g CH_3COONa . This medium was sterilized by autoclaving in bottles at 121 $^\circ\text{C}$ for 20 min. After sterilization, the medium was completed with 8 g/L sodium fumarate filtered at 0.22 μm , 10 mL/L Wolfe's vitamin solution (ATCC MD VS) and 10 mL/L modified Wolfe's minerals (ATCC MD TMS). A pre culture of *G. sulfurreducens* was prepared in a fresh deoxygenated culture medium (2% v/v, 30 $^\circ\text{C}$) for 3 days to reach a final absorbance of around

0.4 at 620 nm. Reactors were then inoculated with this pre culture. The inoculation volume was adjusted to obtain the cell density in each reactor that corresponded to an inoculation ratio of 10% v/v with an inoculum at 0.4 absorbance. Inoculation was performed after 20 min of deoxygenation by bubbling $\text{N}_2:\text{CO}_2$ (80:20) through the reactors filled with the specific growth medium, vitamin solution and modified Wolfe's minerals. In the reactor medium, acetate 10 mM was the sole electron donor and no fumarate was present.

2.3. Experimental set up and electrochemical characterization

All experiments were performed with 3 electrode set ups in single compartment cells. The reactors, each of 500 mL total volume, contained 300 mL solution and were tightly sealed to ensure anaerobic conditions. A gaseous mix of N_2 and CO_2 (80:20) was continuously and gently sparged into each reactor. The gas sparger was located behind the auxiliary electrode and directed towards the reactor wall to avoid disturbance of the working electrode by gas bubbling. The temperature was kept at 30 $^\circ\text{C}$ with a water bath.

The gold electrodes, used as working electrodes, were enclosed in a Teflon based support that exposed a 1 cm^2 surface area to the medium. A platinum grid (Heraeus SAS, Germany) was used as the auxiliary electrode and a saturated calomel reference electrode as the reference (SCE, potential +0.24 V/SHE). Bioanodes were formed under constant polarization at 0.1 V/SCE (VSP potentiostat, Bio Logic SA, France). Current densities were determined based on the projected surface area of the anode, which was always 1 cm^2 . The chronoamperograms were analysed by determining the maximum current density that was reached (J_{max}) and the time required for the electrodes to start to produce current. This starting time was defined as the time at which current density reached 0.1 $\text{A}\cdot\text{m}^{-2}$.

2.4. Microscopy imaging

At the end of the experiments, the bioanodes were stained with acridine orange 0.01% (A6014 Sigma) for 10 min, then carefully washed with medium and dried at ambient temperature. The flat smooth (SG) and nano rough (NG) electrodes were imaged with a Carl Zeiss Axioalger M2 microscope equipped for epifluorescence with an HBO 50 W ac mercury light source and the Zeiss 09 filter (excitor HP450 490, reflector FT 10, Barrier filter LP520). Images were acquired with a monochrome digital camera (Evolution VF). Many different spots were imaged in order to see the general pattern of the colonization.

The micro structured electrodes (μPNG) were imaged with a LEICA TCS SP8 confocal microscope equipped with a 20 W Argon laser and a CS2 UV Optics 1 filter. The active detector was a PMT (500 nm 600 nm). Images were acquired every 2.4 μm along the pillars and the 3D reconstruction was performed using LAS X software.

Epifluorescence images were analysed by greyscale interpretation to calculate the proportion of the electrode surface covered by the bacteria. The grey intensity threshold between the areas covered by the bacteria and the non covered areas was set manually. Grey levels greater than the threshold value were considered to correspond to colonized areas, while grey levels lower than the threshold were considered to show clean areas. Six images, of dimensions 866 by 645 μm , were treated for each electrode to determine the average covering ratio, the edges of the electrodes being excluded to avoid the impact of side effects.

3. Results and Discussion

3.1. Nano structuring

Two smooth (SG) and seven nano rough (NG) gold electrodes were implemented separately in pure cultures of *Geobacter sulfurreducens* under applied potential of 0.1 V/SCE. The medium was fed initially with acetate at 10 mM and sparged continuously with $\text{N}_2:\text{CO}_2$ (80:20).

The smooth electrodes started to produce current at days 3.2 and 5.5 and reached only modest maximum current densities (J_{\max}) of 1.1 and $0.75 \text{ A}\cdot\text{m}^{-2}$ (Fig. 1.A). The nano rough electrodes displayed high variability. Two NG electrodes showed performance close to the SG electrodes: long starting time of 4.2 and 5.1 days, slow current evolution, which led to low J_{\max} of 0.12 and $0.86 \text{ A}\cdot\text{m}^{-2}$ (Fig. 1.B). The other five NG electrodes showed very similar, short starting times between 1 and 1.3 days and reached high J_{\max} values, but with great variability, in a range of 1.6 to $6.4 \text{ A}\cdot\text{m}^{-2}$.

These results reveal a significant variability, particularly relating to J_{\max} , although the initial surfaces and experimental conditions were strictly identical. Nevertheless, they show that the nano roughness of 4.5 nm favoured the electroactive biofilm formation and performance, leading to average J_{\max} of $2.5 \pm 2.0 \text{ A}\cdot\text{m}^{-2}$, in comparison to smooth surface ($R_a = 0.8 \text{ nm}$), which produced average J_{\max} of $0.92 \pm 0.25 \text{ A}\cdot\text{m}^{-2}$.

Once the current had fallen to zero, the electrode colonization was observed by epifluorescence microscopy. Coverage ratios are reported in Table 1. On the two SG electrodes, biofilm clusters had formed and covered 65.8 ± 9.6 and $58.7 \pm 8.7\%$ of the electrode surface as illustrated in Fig. 2.8. Although the global microbial coverage was significant, the biofilm structures were isolated from one another and no large biofilm patches could be observed. On the NG electrodes, as noted for the current production, a wide range of bacterial colonization patterns was observed (Fig. 2.1 to .7). For the two electrodes producing the lowest currents, NG 1 and NG 2, the observation highlighted the presence of microbial colonies and isolated cells on the surface but no significant biofilm patches were observed (Fig. 2.1 and .2). This resulted in coverage ratios of $18.2 \pm 5.2\%$ and $34.2 \pm 10.8\%$. On the NG 3, NG 4 and NG 5 electrodes, producing 1.6 , 2.4 and $2.8 \text{ A}\cdot\text{m}^{-2}$ J_{\max} , the coverage ratios rose to respectively 59.6 ± 8.4 , 77.2 ± 8.7 , and $82.0 \pm 7.0\%$ and biofilm structures were present (Fig. 2.3 to .5). The biofilm did not cover the whole surface continuously but was segmented into patches. On the two highest producing electrodes, NG 6 and NG 7, with J_{\max} of 3.2 and $6 \text{ A}\cdot\text{m}^{-2}$, biofilm covered the whole electrode surface almost uniformly and coverage ratios were 95.2 ± 3.4 and $97.1 \pm 3.9\%$ (Fig. 2.6 and .7). The biofilm observed on the highest producing electrode was thicker and its thickness was uniform, showing a higher maturation of the biofilm structures.

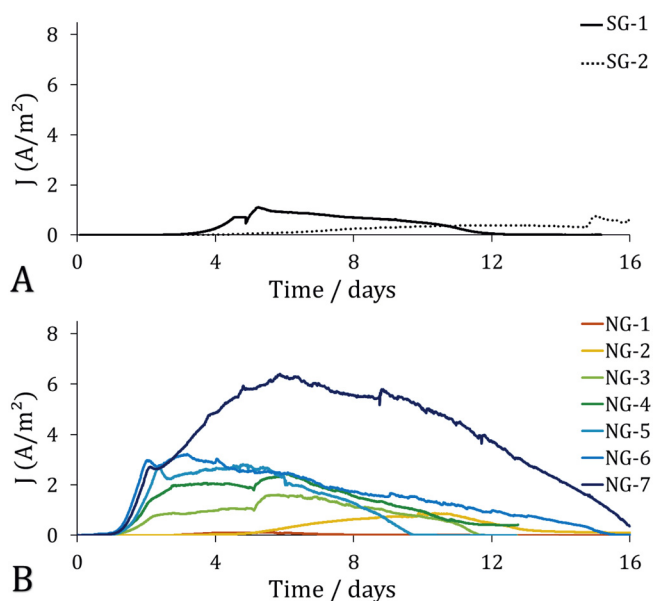


Fig. 1. Chronoamperograms recorded with (A) smooth (SG, $R_a = 0.8 \text{ nm}$) and (B) nano-rough (NG, $R_a = 4.5 \text{ nm}$) gold electrodes under polarization at 0.1 V/SCE with *G. sulfurreducens* and a single batch of acetate 10 mM .

It may be suspected that bacteria that came in contact with the smooth surface ($R_a = 0.8 \text{ nm}$) had great difficulty in linking with it. On such a smooth surface, during the first phase of adhesion, cells were probably entrained away from the surface before achieving an irreversible attachment and starting to create an extracellular matrix. Actually, the shift of the cells from the planktonic to the biofilm (sessile) phenotype is triggered by quorum sensing exchanges [41]. In the case of a smooth surface, the shift to the biofilm phenotype was probably delayed by the slowness of the primary colonization. Smooth surfaces may consequently increase the time needed for an electroactive biofilm to develop. As it was difficult for the cells to adhere to the smooth gold surface, early biofilm development may have mainly taken place by the addition of cells to the few existing micro colonies rather than to the clean surface. In addition, the absence of asperities can also reduce biofilm swarming [42,43]. In consequence, SG electrodes showed isolated biofilm clusters and their shape showed no significant swarming pattern. The smooth surface was a hindrance to biofilm formation during the expansion and connection phase.

In contrast, on the nano rough electrodes, e.g. NG 3 electrode (Fig. 2.3), many small bacterial colonies could be seen, which were all interconnected, thus initiating the formation of good biofilm coverage. The bacterial colonization varied significantly on the different NG surfaces but a clear correlation could be established between the coverage ratio and the maximum current density (Fig. 2). The only electrode that did not show such correlation was the one presenting a mature, uniform biofilm (NG 7). In such cases, the coverage ratio, close to 100%, is no longer the relevant parameter and the biofilm volume should be considered [44]. This relation showed that, in the early stage of electroactive biofilm formation, *G. sulfurreducens* cells were equally efficient for current production whatever their colonization pattern. Small or dense microbial colonies, biofilm patches or uniform biofilm demonstrated the same correlation between coverage ratio and current density produced.

It should be noted that a different type of behaviour has been reported with *G. sulfurreducens* cells colonizing stainless steel cathodes. Increasing the average roughness, R_a , from 2 to $4 \mu\text{m}$ increased current density but, in this case, isolated cells and small colonies were observed to provide higher current density than dense colonies [19]. However, these observations were made in very different conditions from those of the present study: the electrode was operated as a cathode and the electrode material was different. For instance, the semi conductive properties of stainless steel may have impacted the electroactive behaviour of the cells [45]. Moreover, the roughness range was not at the same level: these previous studies dealt with micrometre scale roughness, i.e. roughness that was of similar magnitude to the cell size, while the results presented in this section addressed nanometre roughness. Such different behaviours observed with the same microbial species exposed to different experimental conditions point out the difficulty of extracting universal rules about the early stage formation of electroactive biofilms.

As noted above, the current densities produced by the six NG electrodes exhibited great variability with a standard deviation of $\pm 2.0 \text{ A}\cdot\text{m}^{-2}$ around an average value of $2.5 \text{ A}\cdot\text{m}^{-2}$. Actually, epifluorescence imaging of the electrodes clearly showed that this variability was related to the very different levels of surface colonization. The phase of early microbial settlement on these nano rough, flat surfaces was consequently far from controlled. In contrast, the proportional relationship established between biofilm coverage ratio and current density demonstrated a nice reproducibility of the electron transfer rate that was ensured by cells settled on the electrode surface. The variability observed on the chronoamperograms was due to the early colonization process but, when settled, the microbial cells displayed reproducible electrochemical characteristics.

The correlation between coverage ratio and current production, established here with NG electrodes, was no longer valid for SG electrodes. The SG electrodes showed microbial coverage ratios of 65.8

Table 1

Electrode surface characteristics (roughness and surface area), electrochemical performance and coverage ratios. Maximum current density was calculated with respect to the projected surface area (1 cm^2 for all electrodes) and to the geometric area reported in the third column. Starting time was the time needed to reach $0.1 \text{ A} \cdot \text{m}^{-2}$.

Electrode surface	Roughness Ra (nm)	Geometric area (cm^2)	J_{max} ($\text{A} \cdot \text{m}^{-2}$) projected area	J_{max} ($\text{A} \cdot \text{m}^{-2}$) geometric area	Starting time (days)	Coverage ratio (%)
Smooth	0.8	1	1.1	1.1	3.2	65.8 ± 9.8
			0.75	0.75	5.5	58.7 ± 8.6
Nano-rough	4.5	1	6.4	6.4	1.1	97.1 ± 3.9
			3.2	3.2	1	95.2 ± 3.4
			2.8	2.8	1.2	82.0 ± 7.0
			2.4	2.4	1.1	77.2 ± 8.7
			1.6	1.6	1.3	59.6 ± 8.4
			0.86	0.86	5.1	34.2 ± 10.8
			0.12	0.12	4.2	18.2 ± 5.2
100 μm spaced micropillar	4.5	5.73	8.5	1.48	1.6	97.1 ± 2.8
			8.4	1.48	1.7	95.4 ± 3.1
125 μm spaced micropillar	4.5	5.03	7.5	1.49	1.1	95.1 ± 3.9
			8.2	1.63	1.3	98.3 ± 3.0
200 μm spaced micropillar	4.5	3.26	6.3	1.93	1.1	96.7 ± 2.6
			5.9	1.81	1.2	89.8 ± 3.3

and 58.7% and they produced current densities of $0.92 \text{ A} \cdot \text{m}^{-2}$ on average while, in the same range of biofilm coverage ratios, the NG electrodes produced around twice as much current (Fig. 2). This result suggests that nano roughness may influence the electron transfer rate. The asperities of 4.5 nm on average implemented here may facilitate cell anchoring and, when the cells have settled on the electrode surface, may also improve electron transfer. Nevertheless, further experimental investigations are still required to confirm this hypothesis.

3.2. Surface patterning with micro pillars

Gold electrodes were designed with micro pillars of square cross section $100 \times 100 \mu\text{m}$ and a height of $500 \mu\text{m}$. Three patterns were manufactured with pillar spacings of 100, 125 and $200 \mu\text{m}$, noted μP100NG , μP125NG and μP200NG , respectively. The surface roughness was always 4.5 nm, like that of the nano rough (NG) electrodes used in the previous section. Six μPNG electrodes, two with each pillar spacing, were implemented to form *G. sulfurreducens* anodes. Chronoamperograms displayed a quick start of current production on all electrodes, after between 1.1 and 1.7 days (Fig. 3). The μP100NG , μP125NG and μP200NG electrodes reached maximum current densities of 8.4 , 7.5 and $6.3 \text{ A} \cdot \text{m}^{-2}$, respectively (duplicates gave 8.5 , 8.2 and $5.9 \text{ A} \cdot \text{m}^{-2}$, respectively). These values represent improvements of up to 3.4 fold compared to the average current density provided by the NG electrodes ($2.5 \text{ A} \cdot \text{m}^{-2}$).

The increase in current production obtained with the micro pillar electrodes with respect to the flat NG electrodes was related with the larger surface area created by the addition of the pillars. All the electrodes, both NG and μPNG , had a projected surface area of 1 cm^2 , but the geometric surface area that was really offered to the microbial cells to settle was significantly increased by the addition of the micro pillar arrays. The calculated geometric surface areas were 5.73 cm^2 , 5.06 cm^2 and 3.26 cm^2 with the $100 \mu\text{m}$, $125 \mu\text{m}$ and $200 \mu\text{m}$ spaced micro pillars, respectively (Table 1). The current produced by the micro pillar electrodes varied in the same order as their geometric surface area. Lower pillar spacing led to higher geometric surface area and higher current density.

The current densities can be recalculated with respect to the real geometric area in order to assess the intrinsic efficiency of the biofilms. These "intrinsic" current densities averaged 1.48 , 1.56 and $1.87 \text{ A} \cdot \text{m}^{-2}$ for the μP100NG , μP125NG and μP200NG , respectively (Table 1). Once expressed per unit of real geometric surface area, the biofilm developed on the pillar patterned electrodes produced lower current densities than those developed on the nano rough electrodes ($2.5 \text{ A} \cdot \text{m}^{-2}$).

All the chronoamperograms recorded with the μPNG electrodes exhibited good reproducibility. Although the electrode surfaces of the

μPNG electrodes were made of the same nano rough gold ($R_a = 4.5 \text{ nm}$) as the NG electrodes, the high variability observed with the NG electrodes was no longer observed with the μPNG electrodes. The μ pillar surface patterning considerably decreased the experimental deviation due to microbial adhesion.

Microbial colonization was imaged on the full height of the pillars, from the bottom to the top, by confocal microscopy. It was thus possible to determine that all μPNG electrodes presented coverage ratios above 90% (Fig. 4). The biofilm was well established at the bottom of the electrode and all along the pillars. The biofilm coverage seemed to be close to 100% at the bottom of the pillars but it was not possible to make a numerical measurement to confirm this qualitative observation.

Considering the great height of the micro pillars designed here, with respect to the cell size of a few micrometres or with respect to the height of 8 to $20 \mu\text{m}$ for similar micro structures reported in the literature so far [30,31], it is noteworthy that the biofilm fully covered the bottom interface. The significant height of these pillars did not hamper the full colonization of the electrode surface, right down to their bases. It can now be kept in mind that protruding micro structures intended to increase the surface area available for biofilm development can be of significant height. The ratio of height to separation distance is likely to be a key parameter that should be optimized in order to maximize the interfacial area. Here $500 \mu\text{m}$ high pillars set $100 \mu\text{m}$ apart allowed the biofilm to colonize the pillar sides and the base surface almost uniformly.

The presence of pillars ensured an efficient and reproducible bacterial colonization even though the pillars were covered with the same nano rough gold surface ($R_a = 4.5 \text{ nm}$) as NG electrodes. The great experimental deviation observed on the chronoamperograms with NG electrodes was considerably mitigated by the presence of the micro pillar arrays. A micro pillar array offered a quiet environment for microbial cell adhesion by reducing the local shear stress. In the absence of significant solution stirring, as was the case here, the microbial cells engaged in the micro pillar structure would have difficulty in moving back out. The contact time between the cells and the electrode surface, or the number of contacts, would thus be considerably increased in comparison with those on a fully flat surface, which offers no asperities at the level of a microbial cell size (around $2 \mu\text{m}$). This situation should considerably favour the passage from the reversible adsorption phase to the irreversible phase [46,47].

The great experimental deviation observed with NG electrodes disappeared with μPNG , confirming that these deviations were due to the cell colonization. With μPNG electrodes, the biofilm was well developed on most of the geometric surface area, although the surface area of these electrodes was 3 to 5 times that of the NG electrodes. Surface patterning at the scale of a few hundreds of micrometres was consequently an

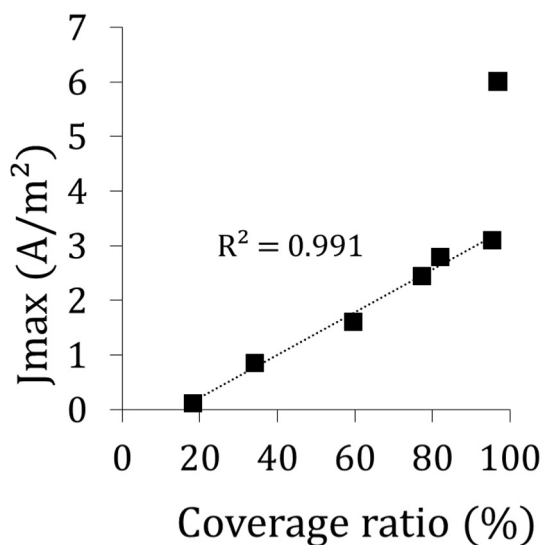
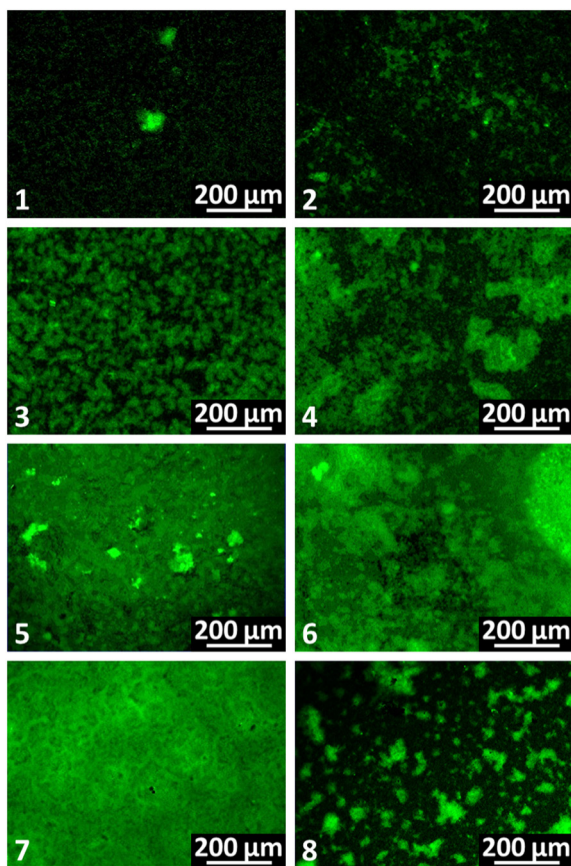


Fig. 2. Correlation between the maximum current density (J_{\max}) obtained with the NG electrodes and their coverage ratio determined by epifluorescence imaging. The epifluorescence pictures presented on the top part are representative of the biofilm coverage observed on (1) NG-1, (2) NG-2, (3) NG-3, (4) NG-4, (5) NG-5, (6) NG-6 and (7) NG-7. The eighth picture (8) is for the smooth gold electrode SG-1.

excellent way to increase the surface area available for biofilm development, on the one hand, and to improve the biofilm formation process, on the other. The μ PNG electrodes thus improved the reproducibility of biofilm formation and subsequently of current production with respect to the NG electrodes, when current densities were calculated with respect to the 1 cm² projected surface area.

Considering the overall geometric surface areas of 5.73, 5.06 and 3.26 cm² the current densities gave J_{\max} of 1.48, 1.56 ± 0.10 and

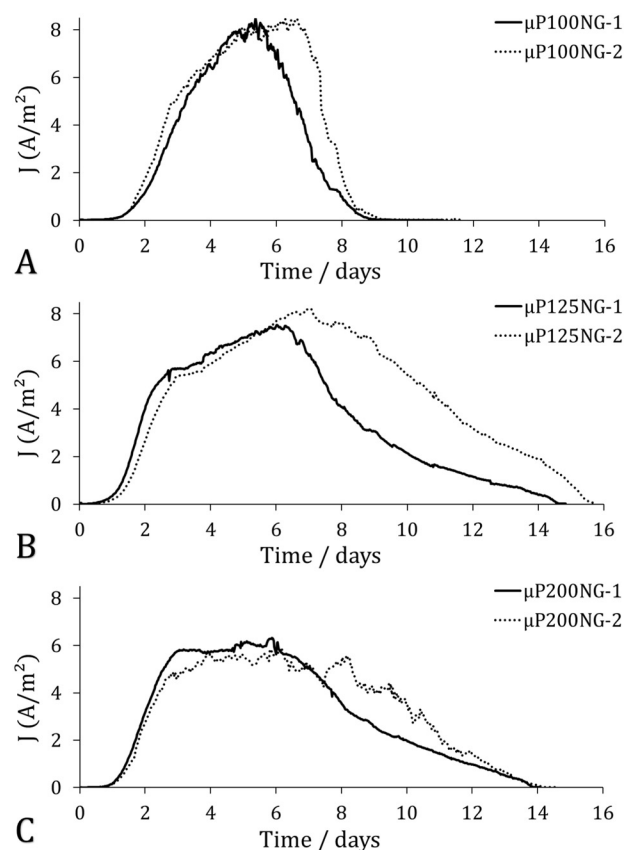
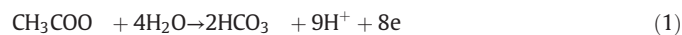


Fig. 3. Chronoamperograms recorded with micro-pillar patterned gold electrodes with different pillar spacings A) 100 μ m (μ P100NG), B) 125 μ m (μ P100NG) and, C) 200 μ m (μ P200NG) under polarization at 0.1 V/SCE with *G. sulfurreducens* and a single batch of acetate 10 mM.

$1.87 \pm 0.10 \text{ A} \cdot \text{m}^{-2}$ for 100, 125 and 200 μ m pillar spacing, respectively (Table 1). As mentioned above, these values were lower than the average current density produced by the NG electrodes. Moreover, considering that the biofilm coverage of the whole geometric surface area of the μ PNG electrodes ranged from 90 to 100%, the correlation in Fig. 2 shows that NG electrodes would produce around $3 \text{ A} \cdot \text{m}^{-2}$ with similar biofilm coverage. This confirms that the μ PNG electrodes produced less current per unit area if the whole geometric surface was considered. Moreover, the 100 μ m spaced pillar array produced the lowest current density and the highest was achieved by the electrodes with pillars 200 μ m apart. These two observations strongly suggest the occurrence of mass transfer limitation, which was more marked with the densest micro pillar array. The diffusion of either acetate or micronutrients, which were in lower concentrations, may have been hampered nearer to the bottom of the micro pillar array. On the other hand, mass transport limitation can also affect the local pH. Acetate oxidation induces local acidification of the electrode:



and acidification is known to be heavily detrimental to anodic electroactive biofilms [48–50]. Local acidification must be mitigated by the diffusion of buffering species from the bulk to the electrode, which may be hampered by the micro pillar array, resulting in pH decrease at the bottom of the micro pillars. It may be pointed out that, at this pH value, protons have no impact on ion transport, as sometimes suggested, but pH is controlled by the migration and diffusion of the buffering species contained in the medium [51]. The hypothesis of mass transport limitation of some compounds, e.g., substrate or buffering species, is consistent with the current plateau, which was observed on

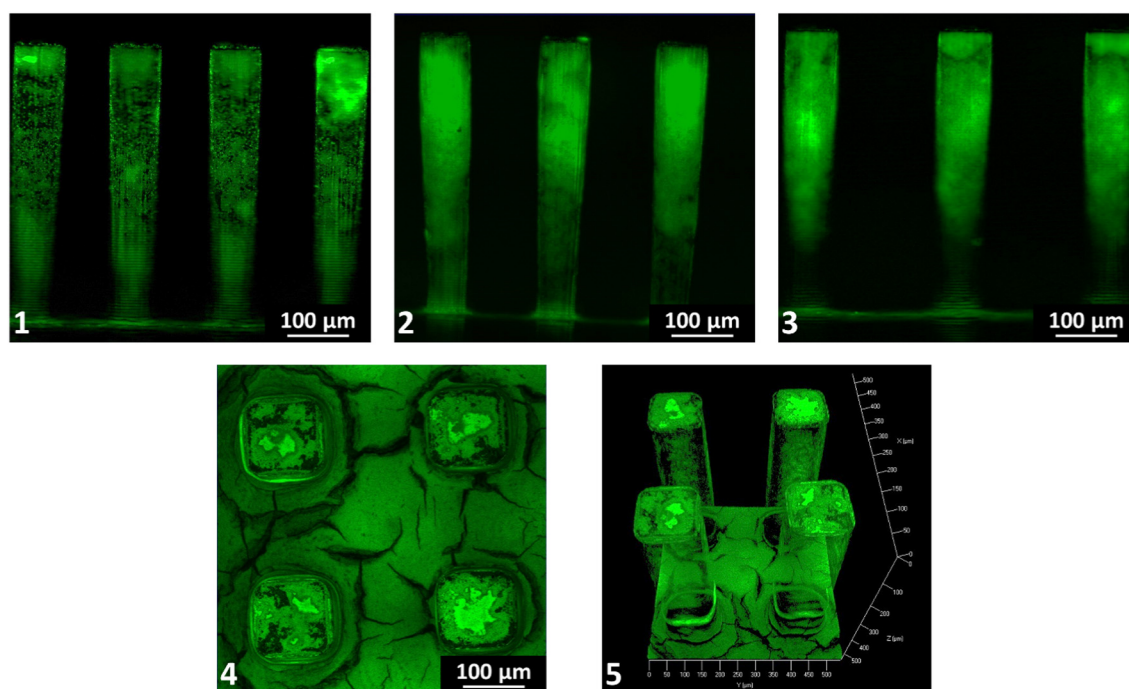


Fig. 4. Epifluorescence pictures of micro-pillar patterned gold electrodes. Side views of (1) $\mu\text{P100NG-1}$, (2) $\mu\text{P125NG-1}$, (3) $\mu\text{P200NG-2}$, (4) and (5) are the top view and a 3D reconstruction of $\mu\text{P125NG-2}$.

the chronoamperograms of the μP200NG electrodes only. With the less dense micro pillar array, the gradient profile resulting from the diffusion/reaction balance was established faster than in the more compact arrays.

3.3. Mass transport beyond the diffusion layer

A simple approach of mass transport modelling is proposed here to assess whether mass transport inside the micro pillar array is a major cause of rate limitation, as supported by the experimental data described above.

The mass transport situation far from the electrode surface must be grasped in order to define the ionic fluxes that reach the front of the electrode. In a general way, mass transport is the result of three contributions: diffusion, migration and convection. In our electrochemical reactors, solution movement was caused only by gentle gas bubbling through a gas disperser, which was deliberately set behind the auxiliary electrodes in order not to disturb the bioanode zone. In such conditions, the convective contribution can be neglected in the bioanode zone. Consequently, outside the diffusion layer of the bioanode, mass transport was mainly ensured by migration. For each ion, the molecular flux driven by migration can be easily calculated by using the transport numbers. The concept of transport numbers and the way to calculate them has been recalled recently in the context of microbial electro technology [51]. The calculation of the ionic composition of the solution used in the electrochemical reactors is described in the Supplementary Information. It led to the transport numbers reported in Table 2.

The transport numbers give the percentage of current that was transported through the solution by the motion of each ionic species. Here, most of the current was transported through the solution by the motion of Na^+ and NH_4^+ to the auxiliary electrode (cathode) and of Cl^- to the bioanode. Using the transport numbers, the molecular balance sheet of the ionic species can be calculated directly. For instance, taking the exchange of 100 electrons as the calculation basis, the molecular flux of each ion is equal to its transport number expressed as a

percentage. It is just necessary to remember to divide the transport number by the charge for multivalent ions (Fig. 5).

When 100 electrons are extracted from the bioanode, 12.5 molecules of acetate are oxidized according to Reaction (1). Migration brings 3.8 molecules of acetate from the bulk to the bioanode. For the process to be stable, 8.7 molecules of acetate must be brought to the bioanode by diffusion.

Moreover, when 100 electrons are extracted from the bioanode, 25 molecules of HCO_3^- and 112.5 protons are produced. To be stable, the process also requires the 112.5 protons be neutralized to avoid local acidification of the bioanode. At pH around neutrality, the concentration of protons is extremely weak. For instance, even accepting significant local acidification to pH 5.0, proton concentration is only 0.01 mM. With such a low concentration, neither migration nor diffusion is efficient to drive the protons away from the interface at a sufficient rate. Protons must consequently be neutralized by the transport of buffering species towards the bioanode. Here, with 112.5 protons produced, 25 at most can be neutralized by the HCO_3^- molecules produced by the reaction. In addition, migration drives 13.6 molecules of HCO_3^- from the bulk to the bioanode together with 0.8 molecules of HPO_4^{2-} , which can also help to neutralize the protons (in the case of divalent ions, the molecular flux is half the charge flux). In total, reaction and migration can neutralize a maximum of 39.4 protons. To be stable, the process requires mass transport by diffusion to bring 73.1 molecules of buffering species to the bioanode.

It can be concluded that migration from the bulk of the solution, far from the electrode surface, did not ensure the mass transport situation that would be required for the bioanode to operate in stable conditions. In such conditions, steep concentration gradients develop close to the electrode surface and diffusion must ensure the majority of mass transport. Here, diffusion must play the main role for the transport of both acetate and the buffering species to the bioanode. Diffusion must bring only 8.7 acetate molecules but 73.1 molecules of buffering species to the bioanode. In consequence, it is much more likely that mass transport limitation appeared because of insufficient diffusion of the buffering species than of substrate.

Table 2

Concentrations and transport numbers of the ionic species contained in the electrochemical reactors after inoculation and pH stabilization by N₂:CO₂ bubbling. Fumarate and succinate came from the pre-culture used as the inoculum (see Supplementary Information).

Ion	Na ⁺	K ⁺	NH ₄ ⁺	HCO ₃	H ₂ PO ₄	HPO ₄ ²⁻	Acetate	Cl	Succinate ²⁻	Fumarate ²⁻
C (mM)	55	1.3	28	29.6	3.6	1.4	9	29.3	4	1
t _i (%)	28.4	1.0	21.2	13.6	1.3	1.6	3.8	23.0	4.8	1.3

3.4. Mass transport through the diffusion layer and inside the micro pillar array

According to the global approach developed in the previous section, diffusion close to the electrode should play the main role in mass transport of the substrate and buffering species.

The impact of diffusion above the micro pillar array can be assessed by assuming a diffusion layer of constant thickness above the micro pillar structure (Fig. 6). In the stationary state, for each species, the diffusion flux, which is driven through the diffusion layer by the concentration gradient, is equal to the flux consumed by the bioanode:

$$-\frac{D}{\delta_{dl}}(C^0 - C^{bulk}) = \frac{J}{nF} \quad (2)$$

where D (m²·s⁻¹) is the diffusion coefficient of the species, δ_{dl} (10⁻⁴ m) is the thickness of the diffusion layer above the micro pillar structure, C^{bulk} and C^0 (mol·m⁻³) are the concentrations in the bulk and at the top of the micro pillar array, J (A·m⁻²) is the current density expressed with respect to the electrode surface area, and F (96 485 C·mol⁻¹) is the Faraday constant.

Dividing by nF transforms the current density into the molar flux of the species consumed by the bioanode. For acetate, n is obviously equal to 8 according to Reaction (1). The case of HCO₃⁻ is slightly more complex. In the stationary state, pH is stable inside the micro pillar structure, so each proton produced by the electrochemical reaction must be extracted by a molecule of HCO₃⁻ that has penetrated into the array and egressed in the form of H₂CO₃. For 8 electrons produced, 9 protons have to be neutralized, but Reaction (1) produces 2 HCO₃⁻ molecules, so only 7 molecules of HCO₃⁻ must penetrate into the array from the bulk, and the parameter n is equal to 8/7.

Calculations were made with current densities J of 8.5 and 6.1 A·m⁻² for micro pillar spacing of 100 and 200 μm, respectively. The diffusion layer thickness was assumed to be 100 μm, which is a common value for an electrochemical process in quiescent solution [52–54]. The diffusion coefficients of acetate and HCO₃⁻ were extracted from the literature. The results reported in Table 3 show a limited impact of the diffusion

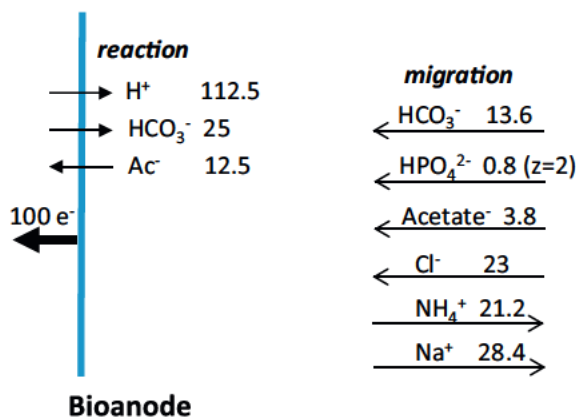


Fig. 5. Molecular balance sheet of the main ionic species involved in charge transport through the bulk on the basis of 100 electrons exchanged. K⁺, H₂PO₄, succinate and fumarate, which had minor roles, are not represented.

layer, diminishing the concentration of acetate from 9 mM in the solution bulk to 8.0 mM at the interface with the top of the micro pillar arrays. Similarly, the concentration decrease was not important for HCO₃⁻, which diminished from 29.6 to 23.1 mM. For both compounds, the maximum gradient was obtained with the 100 μm spacing, which was consistent with the higher current density J produced by this configuration.

Mass transport inside the micro pillar array can be approached by a diffusion reaction equation. The micro pillar pattern offers a highly symmetric topography composed of adjacent elementary units bounded by the central axes of four neighbouring pillars (Fig. 6). The mass transport situation is exactly the same in all these elementary units (i.e. the first derivative of the concentration of each species is nil at the frontier between two adjacent units), so each unit can be modelled as an individual pore. The diffusion reaction equation was established in the x direction perpendicular to the electrode surface in such a unit, i.e. parallel to the micro pillars.

For acetate, the differential mass balance in a section of the elementary unit at the stationary state is:

$$-S D_{Ac} \frac{d^2 C_{Ac}}{dx^2} - I_a \frac{J_{loc}}{nF} \quad (3)$$

where S (m²) is the section of the elementary unit that is free for diffusion, D_{Ac} (m²·s⁻¹) is the diffusion coefficient of acetate, C_{Ac} (mol·m⁻³) is the acetate concentration, I_a (m) is the electrochemically active length in the section of the elementary unit (Fig. 6), J_{loc} (A·m⁻²) is the local current density, i.e. expressed with respect to the overall geometric surface area, $n = 8$ is the number of electrons produced per molecule of acetate consumed (Reaction (1)), and F (96 485 C·mol⁻¹) is the Faraday constant. The width of the micro pillars was always 100 μm, so I_a was equal to 400 μm for all the configurations. In contrast, the free section S depended on the pillar spacing and was equal to (Fig. 6):

$$S = (d + 100 \cdot 10^{-6})^2 - 4 (50 \cdot 10^{-6})^2 \quad (4)$$

where d ($= 100, 125$ or $200 \cdot 10^{-6}$ m) is the distance between pillars.

At the upper surface of the electrode ($x = 0$), the acetate concentration was the interfacial concentration (C_{Ac}^0) calculate above:

$$x = 0, C_{Ac} = C_{Ac}^0 \quad (5)$$

At the bottom of the elementary unit ($x = \delta$), acetate was consumed in the same way as along the electroactive wall:

$$x = \delta, S D_{Ac} \frac{dC_{Ac}}{dx} = -S \frac{J_{loc}}{nF} \quad (6)$$

This assumption was justified by the full biofilm coverage of the bottom of the micro structure electrodes.

To reach a standard approach and reduce the number of parameters to be treated, the equations were transformed into non dimensional form, with the dimensionless variables:

$$\bar{C}_{Ac} = \frac{C_{Ac}}{C_{Ac}^0} \quad \text{and} \quad X = \frac{x}{\delta} \quad (7)$$

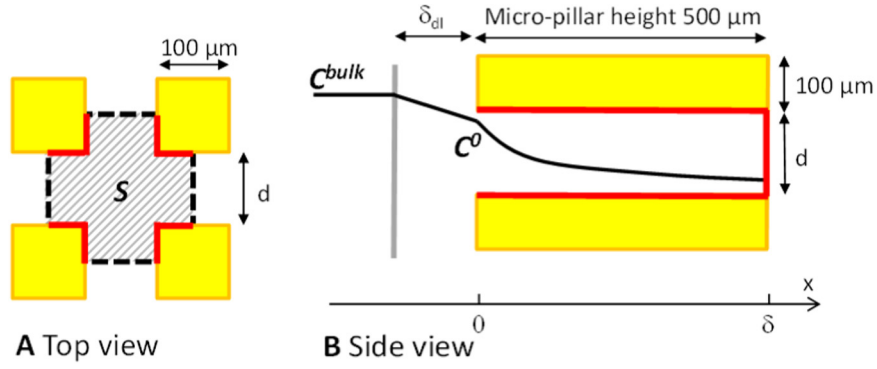


Fig. 6. Scheme of the integration elementary unit. The electroactive length (l_a) is represented by the continuous red line of the frontier; a scheme of concentration profile is represented on the side view.

leading to:

$$\frac{d^2 \bar{C}_{Ac}}{dX^2} - \frac{l_a \delta}{S} \frac{\delta}{D_{Ac} C_{Ac}^0} \frac{J_{loc}}{nF} = 0 \quad (8)$$

$$X = 0, \bar{C}_{Ac} = 1 \quad (9)$$

$$X = 1, \frac{d\bar{C}_{Ac}}{dX} = -\frac{\delta}{D_{Ac} C_{Ac}^0} \frac{J_{loc}}{nF} \quad (10)$$

Two dimensionless numbers appear, one (ζ) is a geometric ratio expressing the overall electrochemically active area in the elementary unit with respect to the section available for diffusion:

$$\zeta = \frac{l_a \delta}{S} \quad (11)$$

the other is the modified Damköhler number [55]:

$$Da_{mod} = \frac{J_{loc}}{nF} \frac{\delta}{D_{Ac} C_{Ac}^0} = \frac{J_{loc}}{nF} \frac{\delta}{D_{Ac} C_{Ac}^0} \quad (12)$$

which expresses the rate of consumption by the electrochemical reaction with respect to the maximum diffusion rate. Solving Eq. (8) with the boundary conditions (9) and (10) gives the concentration profile of acetate in the micro pillar array:

$$\bar{C}_{Ac} = 1 + \zeta Da_{mod} \frac{X^2}{2} - \zeta Da_{mod} \left(\frac{1}{\zeta} + 1 \right) X \quad (13)$$

where X varies from 0 at the top of the micro pillar to 1 at the bottom.

The same equation was derived for HCO_3^- . As detailed above, the current density was transformed into the molar flux of the HCO_3^- that was consumed by the electrochemical reaction by using $n = 8/7$. It may be recalled that, in this context, HCO_3^- was indirectly consumed

by the reaction because, to maintain a stationary state, HCO_3^- is assumed to neutralize the protons produced by the electrochemical reaction (Reaction (1)). This is the condition sine qua non for maintaining a stable pH inside the micro pillar array at the stationary state.

Assuming that HCO_3^- and H_2CO_3 have identical diffusion coefficients, mass conservation indicates that the sum of their concentrations remains equal along the whole diffusion pathway. Calculating the concentration of HCO_3^- along the micro pillars thus directly gives the concentration of H_2CO_3 along the micro pillars and the pH profile with the acid dissociation equilibrium:

$$pH = pKa + \log \left(\frac{C_{HCO_3^-}}{C_{H_2CO_3}} \right) \quad (14)$$

For acetate, the values of ζDa_{mod} (Table 3), were always less than 1, which indicates that the consumption rate by the electrochemical reaction was slower than the maximum diffusion rate (Eq. (12)). The profile of the dimensionless concentration of acetate in the micro pillar array (Fig. 7.A) confirmed that acetate did indeed reach the bottom of the structure and was consequently not a significant source of rate limitation.

The situation was not so obvious for HCO_3^- , which displaced ζDa_{mod} greater than 1 for the 100 μm spaced micro pillars (Table 3). In this case, diffusion may be rate limiting. This was confirmed by the concentration profile (Fig. 7). For the most compact micro pillar array, HCO_3^- did not reach the bottom of the structure. Due to the protons produced by the electrochemical reaction, HCO_3^- was fully consumed at around 80% of the depth of the structure. In this case, HCO_3^- was not able to maintain a stable pH on the whole micro pillar array. The concentration and pH profiles showed that diffusion limitation was not so severe in the 200 μm spaced micro structure. HCO_3^- was able to reach the bottom of the array (Fig. 7). Nevertheless a significant pH gradient occurred inside (Fig. 7), with a value of 5.76 at the bottom.

The pH of the solution bulk was 6.8 and the calculated value was around 6.5 at the top of the micro pillar structure for the two configurations. For the 100 μm spaced micro structure, the model revealed great

Table 3 Parameter values used to model the diffusion of acetate and HCO_3^- through the diffusion layer and inside the micro-pillar arrays. Values of diffusion coefficients from [56]; in all cases $\delta_{dl} = 10^{-4}$ m, $l_a = 4 \cdot 10^{-4}$ m and $\delta = 5 \cdot 10^{-4}$ m.

d	S m^2	J $A \cdot m^{-2}$	J_{loc} $A \cdot m^{-2}$	n	D $m^2 s^{-1}$	C^{bulk} $mol \cdot m^{-3}$	C^0 $mol \cdot m^{-3}$	ζ	Da_{mod}	ζDa_{mod}
Acetate										
100 μm	$3 \cdot 10^{-8}$	8.5	1.48	8	$1.09 \cdot 10^{-9}$	9	8.0	6.67	0.11	0.73
200 μm	$8 \cdot 10^{-8}$	6.1	1.87	8	$1.09 \cdot 10^{-9}$	9	8.3	2.5	0.13	0.34
HCO_3^-										
100 μm	$3 \cdot 10^{-8}$	8.5	1.48	8/7	$1.18 \cdot 10^{-9}$	29.6	23.1	6.67	0.25	1.64
200 μm	$8 \cdot 10^{-8}$	6.1	1.87	8/7	$1.18 \cdot 10^{-9}$	29.6	24.9	2.5	0.29	0.72

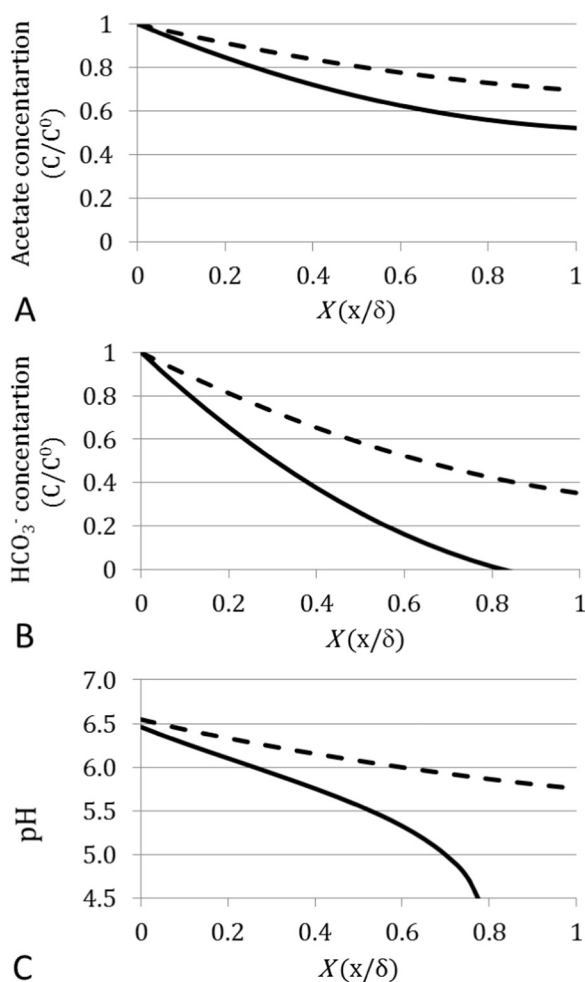


Fig. 7. Theoretical concentration (A and B) and pH (C) profiles inside the micro-pillar arrays calculated by the model with the parameter values given in Table 3, from top ($X = 0$) to bottom ($X = 1$). Continuous line: 100- μm spaced micro-pillars; dashed line: 200- μm spaced micro-pillars.

acidification along the micro pillars, which was probably the main cause of rate limitation. This severe limiting effect explained the low local current density (J_{loc} , expressed with respect to the overall geometric surface area) of $1.48 \text{ A} \cdot \text{m}^{-2}$, while flat electrodes with the same nano roughness and with similar full biofilm coverage produced current densities ranging from 2.5 to $3 \text{ A} \cdot \text{m}^{-2}$ (Fig. 2). Mass transport of the buffering species was less limiting in the case of the 200 μm spaced micro pillars. Nevertheless, a significant pH gradient was calculated, with pH falling to 5.76 at the bottom of the micro pillars. This significant acidification explained why the local current density of $1.87 \text{ A} \cdot \text{m}^{-2}$ was higher than that of the 100 μm spaced structure but did not reach the value of the flat surface.

4. Conclusion

By mastering the roughness of gold surfaces at the nanometre scale, it has been possible to reveal that nano roughness impacts the electron transfer rate of the cells settled on the surface. A roughness of 4.5 nm may improve the electron transfer rate with respect to smooth surface ($R_a = 0.8 \text{ nm}$). Great experimental deviation was observed on the production of current. Nevertheless, regardless of the progress of the microbial colonization on the surface, current density was always directly proportional to the biofilm coverage. The experimental deviations were not due to the electron transfer process but to the difficulty for the microbial cells to settle on flat surfaces.

The experimental reproducibility was considerably improved by patterning the electrode surface with arrays of micro pillars 500 μm in height. The micro pillar array offered the cells an environment that allowed them to establish irreversible adhesion. Moreover, the current density related to the projected surface area was increased around 3.4 fold with respect to the flat electrodes with identical surface roughness (NG electrodes with $R_a = 4.5 \text{ nm}$), because of the larger surface area available for biofilm development.

In conclusion, with respect to the flat smooth surface, nano roughness increased the current density by a factor of 2.8, due to improved electron transfer, and micro structuring improved it by a factor 3.4, due to the area increase. The surface design of microbial electrodes should consequently include nano roughness to favour electron transfer and micro roughness of the order of tens or hundreds of micrometres to increase the surface available for biofilm growth and create a quiet environment favouring cell settlement. The optimal micro roughness must be now designed by balancing the largest possible surface area and the lowest possible mass transport limitation, particularly of the buffering species.

Acknowledgements

This work benefited from the support of the French state, managed by the Agence Nationale de la Recherche (ANR), within the framework of the project Koropokkuru (ANR 14 CE05 0004). The authors would like to acknowledge Luc Etcheverry, Frédéric Dacosta, Jean Pierre Escafit and Vincent Loisel for their help in designing and setting up the reactors as well as Cécile Pouzet (Plateforme Imagerie FR AIB) and Benjamin Erable for their implication in the fluorescence imaging acquisition.

Declaration of interest

None.

Appendix A. Supplementary data

Supplementary data to this article can be found online at <https://doi.org/10.1016/j.bioelechem.2018.02.005>.

References

- H. Wang, Z.J. Ren, A comprehensive review of microbial electrochemical systems as a platform technology, *Biotechnol. Adv.* 31 (2013) 1796–1807, <https://doi.org/10.1016/j.biotechadv.2013.10.001>.
- S. Venkata Mohan, Chapter 6 - Reorienting waste remediation towards harnessing bioenergy: a paradigm shift, in: V.V. Ranade, V.M. Bhandari (Eds.), *Industrial Wastewater Treatment, Recycling and Reuse*, Butterworth-Heinemann, Oxford 2014, pp. 235–281, <https://doi.org/10.1016/B978-0-08-099968-5.00006-4>.
- S. Bajracharya, M. Sharma, G. Mohanakrishna, X. Dominguez Benetton, D.P.B.T.B. Strik, P.M. Sarma, D. Pant, An overview on emerging bioelectrochemical systems (BESs): technology for sustainable electricity, waste remediation, resource recovery, chemical production and beyond, *Renew. Energy* 98 (2016) 153–170, <https://doi.org/10.1016/j.renene.2016.03.002>.
- D.R. Bond, D.E. Holmes, L.M. Tender, D.R. Lovley, Electrode-reducing microorganisms that harvest energy from marine sediments, *Science* 295 (2002) 483–485, <https://doi.org/10.1126/science.1066771>.
- L.M. Tender, C.E. Reimers, H.A. Stecher, D.E. Holmes, D.R. Bond, D.A. Lowy, K. Pilobello, S.J. Fertig, D.R. Lovley, Harnessing microbially generated power on the seafloor, *Nat. Biotechnol.* 20 (2002) 821–825, <https://doi.org/10.1038/nbt716>.
- Y. Zhang, I. Angelidaki, Microbial electrolysis cells turning to be versatile technology: recent advances and future challenges, *Water Res.* 56 (2014) 11–25, <https://doi.org/10.1016/j.watres.2014.02.031>.
- M. Kitching, R. Butler, E. Marsili, Microbial bioelectrosynthesis of hydrogen: current challenges and scale-up, *Enzym. Microb. Technol.* 96 (2017) 1–13, <https://doi.org/10.1016/j.enzmictec.2016.09.002>.
- H. Wang, Z.J. Ren, Bioelectrochemical metal recovery from wastewater: a review, *Water Res.* 66 (2014) 219–232, <https://doi.org/10.1016/j.watres.2014.08.013>.
- Y.V. Nancharaiyah, S. Venkata Mohan, P.N.L. Lens, Metals removal and recovery in bioelectrochemical systems: a review, *Bioresour. Technol.* 195 (2015) 102–114, <https://doi.org/10.1016/j.biortech.2015.06.058>.

- [10] G. Pasternak, J. Greenman, I. Ieropoulos, Self-powered, autonomous biological oxygen demand biosensor for online water quality monitoring, *Sens. Actuators B Chem.* 244 (2017) 815–822, <https://doi.org/10.1016/j.snb.2017.01.019>.
- [11] M. Di Lorenzo, T.P. Curtis, I.M. Head, K. Scott, A single-chamber microbial fuel cell as a biosensor for wastewaters, *Water Res.* 43 (2009) 3145–3154, <https://doi.org/10.1016/j.watres.2009.01.005>.
- [12] B. Erable, L. Etcheverry, A. Bergel, From microbial fuel cell (MFC) to microbial electrochemical snorkel (MES): maximizing chemical oxygen demand (COD) removal from wastewater, *Biofouling* 27 (2011) 319–326, <https://doi.org/10.1080/08927014.2011.564615>.
- [13] B. Matturro, C. Cruz Viggi, F. Aulenta, S. Rossetti, Cable bacteria and the bioelectrochemical snorkel: the natural and engineered facets playing a role in hydrocarbons degradation in marine sediments, *Front. Microbiol.* 8 (2017), <https://doi.org/10.3389/fmicb.2017.00952>.
- [14] W.G. Characklis, K.C. Marshall, *Biofilms*, Wiley, New York, 1990 195–196.
- [15] R.D. Monds, G.A. O'Toole, The developmental model of microbial biofilms: ten years of a paradigm up for review, *Trends Microbiol.* 17 (2009) 73–87, <https://doi.org/10.1016/j.tim.2008.11.001>.
- [16] M. Sun, F. Zhang, Z.-H. Tong, G.-P. Sheng, Y.-Z. Chen, Y. Zhao, Y.-P. Chen, S.-Y. Zhou, G. Liu, Y.-C. Tian, H.-Q. Yu, A gold-sputtered carbon paper as an anode for improved electricity generation from a microbial fuel cell inoculated with *Shewanella oneidensis* MR-1, *Biosens. Bioelectron.* 26 (2010) 338–343, <https://doi.org/10.1016/j.bios.2010.08.010>.
- [17] L. Peng, S.-J. You, J.-Y. Wang, Carbon nanotubes as electrode modifier promoting direct electron transfer from *Shewanella oneidensis*, *Biosens. Bioelectron.* 25 (2010) 1248–1251, <https://doi.org/10.1016/j.bios.2009.10.002>.
- [18] Y. Fan, S. Xu, R. Schaller, J. Jiao, F. Chaplin, H. Liu, Nanoparticle decorated anodes for enhanced current generation in microbial electrochemical cells, *Biosens. Bioelectron.* 26 (2011) 1908–1912, <https://doi.org/10.1016/j.bios.2010.05.006>.
- [19] L. Pons, M.-L. Délia, A. Bergel, Effect of surface roughness, biofilm coverage and biofilm structure on the electrochemical efficiency of microbial cathodes, *Bioresour. Technol.* 102 (2011) 2678–2683, <https://doi.org/10.1016/j.biortech.2010.10.138>.
- [20] D. Poczanoi, A. Calmet, L. Etcheverry, B. Erable, A. Bergel, Stainless steel is a promising electrode material for anodes of microbial fuel cells, *Energy Environ. Sci.* 5 (2012) 9645–9652, <https://doi.org/10.1039/C2EE22429A>.
- [21] C. Feng, F. Li, H. Liu, X. Lang, S. Fan, A dual-chamber microbial fuel cell with conductive film-modified anode and cathode and its application for the neutral electro-Fenton process, *Electrochim. Acta* 55 (2010) 2048–2054, <https://doi.org/10.1016/j.electacta.2009.11.033>.
- [22] Z. Ye, J. Hou, M.W. Ellis, B. Behkam, Effect of anode surface roughness on power generation in microbial fuel cells, *ASME, ASME International Mechanical Engineering Congress and Exposition, Volume 6: Energy, Parts A and B 2012*, pp. 1409–1414, <https://doi.org/10.1115/IMECE2012-88643>.
- [23] K. Guo, B.C. Donose, A.H. Soeriyadi, A. PrévotEAU, S.A. Patil, S. Freguia, J.J. Gooding, K. Rabaey, Flame oxidation of stainless steel felt enhances anodic biofilm formation and current output in bioelectrochemical systems, *Environ. Sci. Technol.* 48 (2014) 7151–7156, <https://doi.org/10.1021/es500720g>.
- [24] X. Jia, Z. He, X. Zhang, X. Tian, Carbon paper electrode modified with TiO₂ nanowires enhancement bioelectricity generation in microbial fuel cell, *Synth. Met.* 215 (2016) 170–175, <https://doi.org/10.1016/j.synthmet.2016.02.015>.
- [25] H. Feng, Y. Liang, K. Guo, W. Chen, D. Shen, L. Huang, Y. Zhou, M. Wang, Y. Long, TiO₂ nanotube arrays modified titanium: a stable, scalable, and cost-effective bioanode for microbial fuel cells, *Environ. Sci. Technol. Lett.* 3 (2016) 420–424, <https://doi.org/10.1021/acs.estlett.6b00410>.
- [26] S. Kalathil, D. Pant, Nanotechnology to rescue bacterial bidirectional extracellular electron transfer in bioelectrochemical systems, *RSC Adv.* 6 (2016) 30582–30597, <https://doi.org/10.1039/c6ra04734c>.
- [27] S. Inoue, E.A. Parra, A. Higa, Y. Jiang, P. Wang, C.R. Buie, J.D. Coates, L. Lin, Structural optimization of contact electrodes in microbial fuel cells for current density enhancements, *Sens. Actuators Phys.* 177 (2012) 30–36, <https://doi.org/10.1016/j.sna.2011.09.023>.
- [28] T. Kano, E. Suito, K. Hishida, N. Miki, Effect of microscale surface geometry of electrodes on performance of microbial fuel cells, *Jpn. J. Appl. Phys.* 51 (2012), 06FK04, <https://doi.org/10.1143/JJAP.51.06FK04>.
- [29] Z. Ye, M.W. Ellis, A.S. Nain, B. Behkam, Effect of electrode sub-micron surface feature size on current generation of *Shewanella oneidensis* in microbial fuel cells, *J. Power Sources* 347 (2017) 270–276, <https://doi.org/10.1016/j.jpowsour.2017.02.032>.
- [30] C.P.B. Siu, M. Chiao, A microfabricated PDMS microbial fuel cell, *J. Microelectromech. Syst.* 17 (2008) 1329–1341, <https://doi.org/10.1109/JMEMS.2008.2006816>.
- [31] J. Kim, Power enhancement of a μ -scale microbial fuel cells by surface roughness, *Appl. Phys. Lett.* 104 (2014), 223702, <https://doi.org/10.1063/1.4880596>.
- [32] C. Dumas, R. Basseguy, A. Bergel, Electrochemical activity of *Geobacter sulfurreducens* biofilms on stainless steel anodes, *Electrochim. Acta* 53 (2008) 5235–5241, <https://doi.org/10.1016/j.electacta.2008.02.056>.
- [33] A. Baudler, I. Schmidt, M. Langner, A. Greiner, U. Schröder, Does it have to be carbon? Metal anodes in microbial fuel cells and related bioelectrochemical systems, *Energy Environ. Sci.* 8 (2015) 2048–2055, <https://doi.org/10.1039/C5EE00866B>.
- [34] H. Richter, K. McCarthy, K.P. Nevin, J.P. Johnson, V.M. Rotello, D.R. Lovley, Electricity generation by *Geobacter sulfurreducens* attached to gold electrodes, *Langmuir* 24 (2008) 4376–4379, <https://doi.org/10.1021/la703469y>.
- [35] Y. Liu, H. Kim, R. Franklin, D.R. Bond, Gold line array electrodes increase substrate affinity and current density of electricity-producing *G. sulfurreducens* biofilms, *Energy Environ. Sci.* 3 (2010) 1782–1788, <https://doi.org/10.1039/C0EE00242A>.
- [36] N.S. Malvankar, M. Vargas, K.P. Nevin, A.E. Franks, C. Leang, B.-C. Kim, K. Inoue, T. Mester, S.F. Covalla, J.P. Johnson, V.M. Rotello, M.T. Tuominen, D.R. Lovley, Tunable metallic-like conductivity in microbial nanowire networks, *Nat. Nanotechnol.* 6 (2011) 573–579, <https://doi.org/10.1038/nnano.2011.119>.
- [37] C. Koch, F. Harnisch, Is there a specific ecological niche for electroactive microorgan-isms? *ChemElectroChem.* 3 (2016) 1282–1295, <https://doi.org/10.1002/celec.201600079>.
- [38] D.R. Bond, D.R. Lovley, Electricity production by *Geobacter sulfurreducens* attached to electrodes, *Appl. Environ. Microbiol.* 69 (2003) 1548–1555, <https://doi.org/10.1128/AEM.69.3.1548-1555.2003>.
- [39] D.R. Lovley, T. Ueki, T. Zhang, N.S. Malvankar, P.M. Shrestha, K.A. Flanagan, M. Aklujkar, J.E. Butler, L. Giloteaux, A.-E. Rotaru, D.E. Holmes, A.E. Franks, R. Orellana, C. Riso, K.P. Nevin, *Geobacter*: the microbe electric's physiology, ecology, and practical applications, *Adv. Microb. Physiol.* 59 (2011) 1–100, <https://doi.org/10.1016/B978-0-12-387661-4.00004-5>.
- [40] L. Soussan, B. Erable, M.-L. Delia, A. Bergel, The open circuit potential of *Geobacter sulfurreducens* bioanodes depends on the electrochemical adaptation of the strain, *Electrochem. Commun.* 33 (2013) 35–38, <https://doi.org/10.1016/j.elecom.2013.04.013>.
- [41] Y. Irie, M.R. Parsek, Quorum sensing and microbial biofilms, in: T. Romeo (Ed.), *Bacterial Biofilms*, Springer-Verlag, Berlin, Berlin 2008, pp. 67–84, https://doi.org/10.1007/978-3-540-75418-3_4.
- [42] E. Medilanski, K. Kaufmann, L.Y. Wick, O. Wanner, H. Harms, Influence of the surface topography of stainless steel on bacterial adhesion, *Biofouling* 18 (2002) 193–203, <https://doi.org/10.1080/08927010290011370>.
- [43] D. Rodriguez, B. Einarsson, A. Carpio, Biofilm growth on rugose surfaces, *Phys. Rev. E* 86 (2012), 061914, <https://doi.org/10.1103/PhysRevE.86.061914>.
- [44] E. Blanchet, B. Erable, M.-L. De Solan, A. Bergel, Two-dimensional carbon cloth and three-dimensional carbon felt perform similarly to form bioanode fed with food waste, *Electrochem. Commun.* 66 (2016) 38–41, <https://doi.org/10.1016/j.elecom.2016.02.017>.
- [45] L. Pons, M.-L. Délia, R. Basséguy, A. Bergel, Effect of the semi-conductive properties of the passive layer on the current provided by stainless steel microbial cathodes, *Electrochim. Acta* 56 (2011) 2682–2688, <https://doi.org/10.1016/j.electacta.2010.12.039>.
- [46] R. Belas, Sensing, response, and adaptation to surfaces: swarmer cell differentiation and behavior, in: M. Fletcher (Ed.), *Bacterial Adhesion: Molecular and Ecological Diversity*, Wiley, New York, 1996 <https://doi.org/10.1002/maco.19970480916>.
- [47] E. Karatan, P. Watnick, Signals, regulatory networks, and materials that build and break bacterial biofilms, *Microbiol. Mol. Biol. Rev.* 73 (2009) 310–347, <https://doi.org/10.1128/MMBR.00041-08>.
- [48] S.C. Popat, C.I. Torres, Critical transport rates that limit the performance of microbial electrochemistry technologies, *Bioresour. Technol.* 215 (2016) 265–273, <https://doi.org/10.1016/j.biortech.2016.04.136>.
- [49] B.G. Lusk, P. Parameswaran, S.C. Popat, B.E. Rittmann, C.I. Torres, The effect of pH and buffer concentration on anode biofilms of *Thermincola ferriacetica*, *Bioelectrochemistry* 112 (2016) 47–52, <https://doi.org/10.1016/j.bioelechem.2016.07.007>.
- [50] A.K. Marcus, C.I. Torres, B.E. Rittmann, Analysis of a microbial electrochemical cell using the proton condition in biofilm (PCBIOFILM) model, *Bioresour. Technol.* 102 (2011) 253–262, <https://doi.org/10.1016/j.biortech.2010.03.100>.
- [51] M. Oliot, S. Galier, H. Roux de Balman, A. Bergel, Ion transport in microbial fuel cells: key roles, theory and critical review, *Appl. Energy* 183 (2016) 1682–1704, <https://doi.org/10.1016/j.apenergy.2016.09.043>.
- [52] S.C. Dexter, S.H. Lin, Calculation of seawater pH at polarized metal surfaces in the presence of surface films, *Corrosion* 48 (1992) 50–60, <https://doi.org/10.5006/1.3315918>.
- [53] A.G. Zelinsky, B.Y. Pirogov, Effective thickness of the diffusion layer during hydrogen ion reduction in aqueous hydrochloric acid solutions, *Russ. J. Electrochem.* 44 (2008) 585–593, <https://doi.org/10.1134/S1023193508050133>.
- [54] V.S. Bagotsky (Ed.), *Mass Transfer in Electrolytes*, in: *Fundamental Electrochemistry*, John Wiley & Sons, Inc. 2005, pp. 51–67, <https://doi.org/10.1002/047174199X.ch4>.
- [55] K. Scott, Y.-P. Sun, Approximate analytical solutions for models of three-dimensional electrodes by Adomian's decomposition method, in: C.G. Vayenas (Ed.), *Modern Aspects of Electrochemistry n°39*, Springer, New York 2007, pp. 221–304, https://doi.org/10.1007/978-0-387-46108-3_4.
- [56] J.R. Rumble (Ed.), *CRC Handbook of Chemistry and Physics*, 98th Edition CRC Press/Taylor & Francis, Boca Raton, 2018 (ISBN 9781498784542).

Effect of surface nano/micro-structuring on the early formation of microbial anodes with *Geobacter sulfurreducens*: experimental and theoretical approaches

Supplementary information

Pierre Champigneux ^{a*}, Cyril Renault-Sentenac ^b, David Bourrier ^b, Carole Rossi ^b, Marie-Line Delia ^a, Alain Bergel ^a

^a *Laboratoire de Génie Chimique CNRS - Université de Toulouse (INPT), 4 allée Emile Monso, 31432 Toulouse, France*

^b *Laboratoire d'Analyse et d'Architecture des Systèmes CNRS – Université de Toulouse, 7 avenue du colonel Roche 31031 Toulouse, France*

Calculation of the ionic composition and the transport numbers of the solution implemented in the electrochemical reactors.

The inoculum was prepared by pre-culturing the *G. sulfurreducens* cells with sodium acetate (CH₃COONa) 10 mM, used as the electron donor, and sodium fumarate (Na₂C₄H₂O₄) 50 mM, used as the electron acceptor. Acetate was oxidized into hydrogen carbonate, producing 8 electrons per molecule:



and fumarate was reduced to succinate, consuming 2 electrons per molecule:



Considering the electron balance, the overall transformation was:



Assuming that acetate was completely oxidized at the end of the pre-culture, the samples used for inoculating the electrochemical reactors contained sodium hydrogen carbonate 10 mM, succinate 40

mM, with 10 mM fumarate remaining. Actually, to be fully rigorous, the ratio between HCO_3^- and H_2CO_3 should be calculated as a function of the pH, including the equilibrium of the phosphate species contained in the medium and the possible dissolution of CO_2 from the gas. Nevertheless, this correction would have had a very minor impact on the assessment of the concentrations of the major ions that composed the solution in the electrochemical reactors.

Before inoculation, the solution in the electrochemical reactors was the same as the medium used for the cell pre-culture except that fumarate was omitted to force the cells to use the electrode as the sole electron acceptor. This composition is recalled in the first column of Table 1. Inoculating with the pre-culture at a 10% (v/v) ratio modified the initial composition of the solution because of the presence of additional compounds in the inoculum sample (hydrogen carbonate, fumarate and succinate) and the absence of some others (acetate). The concentrations in the electrochemical reactors after inoculation are reported in column 2 of Table 1. The columns to the right give the contribution of each component in terms of ionic species.

Table 1. Composition of the solution in the electrochemical reactors before (first column) and after (second column) inoculation with the cell pre-culture (10% v/v). Micro-nutriments and vitamins have been omitted. The 10 columns to the right give the contribution of each compound to the ionic concentration after inoculation.

	Initial Medium (mM)	After inoc. (mM)	Ionic contribution after inoculation (mM)											
			Na^+	K^+	NH_4^+	HCO_3^-	H_2PO_4^-	HPO_4^{2-}	Acet $^-$	Cl $^-$	Suc $^{2-}$	Fum $^{2-}$		
NaHCO ₃	30	31	31			31*								
NH ₄ Cl	28	28			28					28				
CH ₃ COO	10	9	9						9					
NaH ₂ PO ₄	5	5	5					total : 5						
KCl	1.3	1.3		1.3						1.3				
C ₄ H ₂ O ₄ Na	0	1	2											1
C ₄ H ₄ O ₄ Na	0	4	8									4		
ion concentration after inoculation (mM)			55	1.3	28	31*		total : 5	9	29.3	4	1		
ion concentration after pH adjustment with N₂:CO₂ (mM)			55	1.3	28	29.6	3.6	1.4	9	29.3	4	1		
transport number (%)			28.4	1	21.2	13.6	1.3	1.6	3.8	23	4.8	1.3		

* A part of the carbonate species should be in non-dissociated form, H_2CO_3

The phosphate and carbonate compounds were initially brought into the solution only in the forms of H_2PO_4^- and HCO_3^- , respectively. The ratios between the species H_2PO_4^- and HPO_4^{2-} and HCO_3^- and H_2CO_3 were then controlled by the pH of the solution. The pH was maintained at 6.8 by constant bubbling of $\text{N}_2:\text{CO}_2$. The concentrations of H_2PO_4^- and HPO_4^{2-} were calculated by using the acid dissociation constant:

$$10^{-7.2} = \frac{HPO_4^{2-} H^+}{H_2PO_4^-} \quad (4)$$

which led, at pH 6.8, to HPO_4^{2-} 1.4 mM and $H_2PO_4^-$ 3.6 mM, giving the total phosphate concentration of 5 mM (Table 1). Then, the concentration of HCO_3^- , which had been disturbed by CO_2 gas bubbling, was corrected by using the overall charge balance:

$$\begin{aligned} & [HCO_3^-] + [H_2PO_4^-] + 2[HPO_4^{2-}] + [Acetate^-] + [Cl^-] + 2[Succinate^{2-}] + 2[Fumarate^{2-}] \\ & = [Na^+] + [K^+] + [NH_4^+] \end{aligned} \quad (5)$$

Assuming that acetate, succinate and fumarate were in their fully dissociated forms led to a concentration of HCO_3^- of 29.6 mM. The HCO_3^-/H_2CO_3 acid dissociation constant ($pK_a = 6.3$) indicated that the concentration of H_2CO_3 was 9.4 mM. The total concentration of the carbonate species, when the pH was stabilized at 6.8 by gas bubbling, was consequently 39 mM. Gas bubbling was responsible for an increase of 8 mM of the concentration of the carbonate species.

These concentration values were then used to calculate the transport number (t_i) of each ionic species expressed as [1]:

$$t_i = \frac{\lambda_i C_i}{\sum_k \lambda_k C_k} \quad (6)$$

where λ_i is the molar ionic conductivity ($m^2.S.mol^{-1}$) and C_i the concentration ($mol.m^{-3}$) of species i . The transport numbers reported in the last line of Table 1 were calculated with the values of molar ionic conductivities extracted from the literature and reported in Table 2.

Table 2. Molar ionic conductivities from [2]

Ion	Na ⁺	K ⁺	NH ₄ ⁺	HCO ₃ ⁻	H ₂ PO ₄ ⁻	HPO ₄ ²⁻	Acetate ⁻	Cl ⁻	Succinate ²⁻	Fumarate ²⁻
λ_i (10 ⁻⁴ m ² S mol ⁻¹)	50.1	73.5	73.5	44.5	36	114	40.9	76.3	117.6	123.6

Acknowledgements

This work benefited from the support of the French state, managed by the Agence Nationale de la Recherche (ANR), within the framework of the project Koropokkuru (ANR-14-CE05-0004).

References

- [1] M. Olliot, S. Galier, H. Roux de Balman, A. Bergel, Ion transport in microbial fuel cells: Key roles, theory and critical review, *Appl. Energy*. 183 (2016) 1682–1704. doi:10.1016/j.apenergy.2016.09.043.
- [2] J.R. Rumble, ed., *CRC Handbook of Chemistry and Physics*, 98th Edition (Internet Version 2018), CRC Press/Taylor & Francis, Boca Raton, FL.